

The Strong Confinement Regime in HgTe Two-Dimensional Nanoplatelets

Nicolas Moghaddam, Charlie Gréboval, Junling Qu, Audrey Chu, Prachi Rastogi, Clément Livache, Adrien Khalili, Xiang Zhen Xu, Benoit Baptiste, Stefan Klotz, Guy Fishman, Francesco Capitani, Sandrine Ithurria, Sébastien Sauvage,* and Emmanuel Lhuillier*

Cite This: *J. Phys. Chem. C* 2020, 124, 23460–23468

Read Online

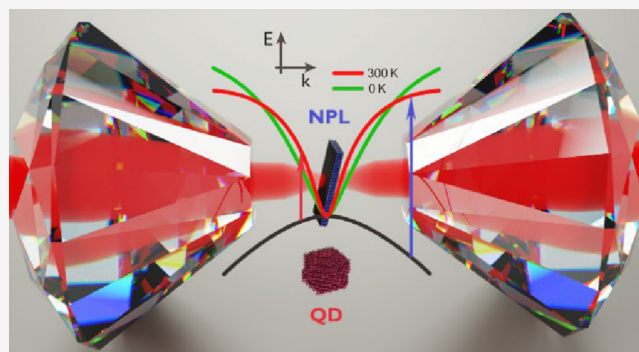
ACCESS |

Metrics & More

Article Recommendations

Supporting Information

ABSTRACT: The confinement in colloidal HgTe nanocrystals enables this material to be promising for colloidal optoelectronics over a wide range of energies, from the THz spectral range up to the visible region. Herein, using a combination of high-energy-absorption HgTe nanoplatelets and low-energy-absorption HgTe nanocrystals, we probe the optical transmission of HgTe nanoparticles over the 0.26–1.8 eV range, from 0 to 300 K temperatures and under simultaneous pressure, up to 4 GPa. While the pressure dependence of nanoplatelets follows the one observed for bulk and nanocrystals, the temperature dependence dramatically differs for nanoplatelets. The modeling of the electronic energy dispersion using up to 14-band $\mathbf{k}\cdot\mathbf{p}$ formalism suggests that the second conduction band and higher bands of HgTe play a vital role in describing and explaining the HgTe nanoparticle spectroscopies.



INTRODUCTION

In bulk semiconductors, spectral tunability relies on material alloying with a second compound. This alloying condition can become a challenge when lattice-matched thin films need to be grown on a given substrate. In nanocrystals (NCs), quantum confinement offers an alternative method to achieve spectral control. This approach is nowadays used to generate green and red light for displays¹ using CdSe or InP as active materials. In such an application, the confinement-induced renormalization of the band gap corresponds to a few tens of percent. Over the past decade, infrared optoelectronics² has also generated interest with applications such as solar cells^{3,4} and low-cost infrared (IR) sensors^{5–9} including focal plane arrays.^{10–12} For these IR applications, narrow band gap materials, such as lead and mercury chalcogenides, are used, and the relative change of the band gap resulting from confinement is even more important. Thus, the lowest-energy optical feature of HgTe can be tuned from the THz^{13,14} to the visible range (i.e., over two orders of magnitude of energy) only using confinement, due to the lack of bulk band gap. To obtain such tunability, the particle size needs to be tuned from a few monolayers (MLs) in HgTe two-dimensional (2D) nanoplatelets (≈ 1 nm thickness)^{15,16} (NPLs) to ≈ 1 μm diameter in bulk-like nanocrystals.¹⁴ The resulting change of confinement corresponds to very different ranges of wavevectors in the energy dispersion of the bulk material. This raises the need for an

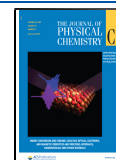
accurate modeling of the energy dispersion all over the Brillouin zone.

The electronic structure of the bulk Hg(Cd)Te attracted significant interests in the 80s–90s owing to the use of this material for IR sensing.^{17,18} Bulk HgTe is a vanishing band gap semiconductor with an inverted band ordering, see Figure 1.¹⁹ Recently, the material has regained some interest as the first example of a topological insulator.²⁰ In the latter case, a barely confined quantum well of HgTe is sandwiched within a CdTe matrix and presents edge channels for transport, as the bands recover their normal ordering at the interface.^{21,22} For zero-dimensional (0D) NCs, the electronic spectrum has been deeply investigated using infrared spectroscopy to measure the absorption cross-section,²³ or to reveal the exciton fine structure.^{24,25} Complementary, the electronic spectrum of weakly confined HgTe NCs has been modeled using the two-band $\mathbf{k}\cdot\mathbf{p}$ formalism²⁴ and the tight-binding method.^{26,27} However, very little work has been devoted to the most strongly confined form of HgTe such as the one obtained in

Received: August 18, 2020

Revised: September 23, 2020

Published: September 24, 2020



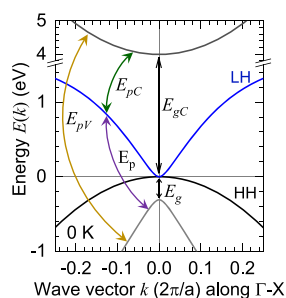


Figure 1. Dispersion relation $E(k)$ of the LH conduction (blue) and HH valence (black) bands of bulk HgTe from the (3 + 1) band $k\cdot p$ model.

HgTe 2D NPLs where the confinement energy can be as large as 1.5 eV.

This lack appears to be detrimental since device progresses appear to be strongly correlated to a deeper understanding of the material and its electronic structure. For the sake of illustration, systematic measurements of the band alignment^{10,24,28} in HgTe NCs have enabled the design of unipolar barriers²⁸ to reduce the device dark current. Alternatively, the development of HgTe-based colloidal heterostructures not only appears promising to expand the range of wavelengths reachable by the 2D NPLs^{29,30} but also raises questions relative to the understanding of the optical spectrum to disentangle charge delocalization effect from pressure effect resulting from nonlattice-matched shells.³¹

In this paper, we explore in a systematic way the effect of confinement, temperature, and pressure on the energy dispersion of HgTe. In practice, we grow a series of HgTe NCs with various confinement energies from 0.26 to 1.8 eV. The temperature is tuned from 0 to 300 K which corresponds to cryogenic operating conditions for IR sensors, and finally, the pressure is tuned up to 4 GPa, corresponding to the full range of existence of the zinc-blende low-pressure phase of HgTe nanoparticles. While the pressure dependence of the spectroscopic properties appears to be weakly affected by the confinement, we show that the temperature dependence of the 2D NPLs is opposite to the one observed for bulk and weakly confined NCs. Our multiband $k\cdot p$ modeling points to the central role of the second conduction band in the origin of this observation. Finally, using a 14-band $k\cdot p$ model, we are able to propose a set of parameters that correctly account for temperature and pressure dependence and describe the dispersion relation of HgTe over an extended range of the Brillouin zone.

METHODS

Chemicals. Mercury chloride (HgCl_2 , Strem Chemicals, 99%) and $\text{Hg}(\text{Acetate})_2$ ($\text{Hg}(\text{Ac})_2$, Aldrich, > 99.0%); **mercury compounds are highly toxic. Handle them with special care.** Tellurium powder (Te, Sigma-Aldrich, 99.99%), cadmium oxide (CdO) (Aldrich 99.99%), trioctylphosphine (TOP) (Alfa, 90%), oleic acid (OA, Sigma, 90%), propionic acid (Aldrich, 99%), oleylamine (OLA, Acros, 80–90%), dodecanethiol (DDT, Sigma-Aldrich, 98%), trioctylamine (TOA, Aldrich), octadecene (ODE) (Aldrich, 90%), chloroform (Carlo Erba), methanol (VWR, 98.5%), acetone (VWR rechapur), ethanol (absolute VWR), and toluene (VWR, 99.8%). All chemicals are used without further purification.

Cadmium Propionate ($\text{Cd}(\text{prop})_2$). CdO (1.036 g) is mixed in 10 mL of propionic acid under Ar for 1 h. Then, the flask is opened and exposed to air, and the temperature is raised to 140 °C up to the point the volume gets divided by a factor of 2. The whitish solution is precipitated by the addition of acetone. After centrifugation, the solid is dried under vacuum for 24 h.

1 M TOP:Te Precursor. Te powder (2.54 g) is mixed in 20 mL of TOP in a three-neck flask. The flask is kept under vacuum at room temperature for 5 min and then the temperature is raised to 100 °C. Furthermore, the degassing of the flask is conducted for the next 20 min. The atmosphere is switched to Ar, and the temperature is raised to 275 °C. The solution is stirred until a clear orange coloration is obtained. The flask is cooled down to room temperature, and the color switches to yellow. Finally, this solution is transferred to an Ar-filled glovebox for storage.

Synthesis of 3 MLs CdTe NPLs. The procedure follows the method proposed by Pedetti et al.³² In a three-neck flask, $\text{Cd}(\text{prop})_2$ (390 mg, 1.5 mmol), oleic acid (240 μL , 0.75 mmol), and 30 mL of octadecene are degassed under vacuum at 90 °C for 1 h. Under argon flow, TOP:Te at 1 M (300 μL) diluted in 1.5 mL of octadecene is swiftly injected at 210 °C. After 30 min of reaction, the mixture is cooled down and 1.7 mL of oleic acid is introduced. The resulting nanoplatelets are precipitated twice with an excess of ethanol and then are redispersed in 30 mL of hexane.

Cation Exchange for the Synthesis of 3 MLs HgTe NPLs with TOA. In a glass tube, 2 mL of hexane and 200 μL of CdTe NPLs are introduced. A volume of 60 μL of fresh 0.1 M HgAc_2 in trioctylamine solution is added at room temperature (The Cd:Hg ratio is 1:2). The cation exchange is followed by absorption spectroscopy. Once the first excitonic peak has reached 824 nm, 80 μL of oleic acid is added to stabilize the HgTe NPLs. The excess of precursors is removed by centrifugation. The resulting NPLs are resuspended in 1 mL of toluene. Procedures for other surface chemistries on the HgTe NPL surface are given in the Supporting Information.

HgTe NCs Synthesis with Band Edge at 4000 cm^{-1} . HgCl_2 (513 mg) was added to 60 mL of oleylamine in a 100 mL round flask. The solution was placed under vacuum and heated to 110 °C for 1 h. Then, the temperature is decreased to 80 °C and the solution is placed in a N_2 atmosphere. A volume of 1.9 mL of TOP:Te (1 M) with 10 mL of oleylamine is added to the mercury solution. The solution color gradually turns to dark brown, and the reaction is stopped after 3 min. A solution made of 1 mL of dodecanethiol and 9 mL of toluene is quickly added to quench the reaction. The nanocrystals are then precipitated with ethanol. After centrifugation, the nanocrystals are redispersed in chloroform. The washing step is repeated one more time. The solution is filtered with a 0.2 μm filter and redispersed in 6 mL of chloroform. Procedures for other NC sizes are given in the Supporting Information.

Electron Microscopy. For transmission electron microscopy (TEM) pictures, a drop of the NC solution is drop-cast onto a copper grid covered with an amorphous carbon film. The grid is degassed overnight to reduce future contamination. A JEOL 2010F is used for the acquisition of pictures and operated at 200 kV.

Infrared Spectroscopy as a Function of Temperature. The solution of the nanocrystal is drop-casted onto a double side polished Si wafer for the sample in the mid-infrared and onto a CaF_2 substrate for the sample in the near-infrared. The

Table 1. Values of the Simple (3 + 1) and the 14-Band Model Parameters Used to Describe the Confinement, Temperature, and Pressure Dependences^a

parameter	simple (3 + 1)-band model value	14-band k _p model value	reference
E_g^0	0.31 eV	0.375 eV	0.303 eV in ref 55.
simulated $E_g(k = 0)$		0.305 eV	
E_{gC}^0	4 eV	2.5 eV	4.11 eV (QSGW) and 3.07 eV (LDA) in ref 51.
simulated $E_{gC}(k = 0)$		2.78 eV	
E_p	25 eV	30 eV	fitted, 24.8 eV in ref 55.
E_{pC}	15 eV	20 eV	fitted
E_{pV}	2.5 eV	10 eV	fitted
$\partial E_g / \partial T$	from $E_g(T, P)$, typically ≈ -0.61 meV.K ⁻¹	from $E_g(T, P)$ plus a constant 0.1 meV.K ⁻¹ , typically ≈ -0.51 meV.K ⁻¹	see $E_g(T, P)$ formula in Supporting Information
$\partial E_{gC} / \partial T$	-2.4 meV.K ⁻¹	-3 meV.K ⁻¹	fitted
$\partial E_g / \partial P$	-85 meV/GPa	-95 meV/GPa	fitted
$\partial E_{gC} / \partial P$	+220 meV/GPa	+600 meV/GPa	fitted
a bulk HgTe lattice parameter	0.6465 nm		ref 34 at 300 K
a_0^{NP} HgTe nanoparticle lattice parameter	0.6500 nm		from measurement on NPLs at 300 K, Figure S6c
B_0 HgTe nanoparticle elasticity modulus	30 GPa		from measurement on NPLs at 300 K, Figure S6c
$\partial B_0 / \partial P$	-1.5		from measurement on NPLs at 300 K, Figure S6c
m_{LH}^*	0.013 m_0	0.013 m_0	output
m_{HH}^*	0.33 m_0	0.69 m_0	output
spin-orbit coupling Δ	n.a.	0.5 eV	0.775 eV (hQSGW) in ref 51.
simulated spin-orbit coupling at $k = 0$	n.a.	0.732 eV	1.08 eV in ref 51.
Δ_C	n.a.	1 eV	1.06 eV (QSGW) 1.17 eV (LDA) in ref 51.
simulated spin-orbit coupling at $k = 0$	n.a.	0.768 eV	
Δ'	n.a.	-1.5 eV	fitted

^an.a. means nonapplicable.

sample is mounted on the cold finger of a closed-cycle cryostat. The latter is used in a transmission configuration with two ZnSe windows. The cryostat is then introduced into the Fourier transform infrared spectrometer (FTIR, Thermo Fischer iS 50). Two sources have been used: a white light in the near-infrared and a globar in the mid-infrared. Two beam splitters have been used: a CaF₂ beam splitter in the near-infrared and an extended KBr one in the mid-infrared. Two detectors have been used: an InGaAs sensor in the near-infrared and a DTGS one in the mid-infrared. In all the cases, the background is made at room temperature using the same optical configuration but without sample onto the substrate. Spectra are acquired with a 4 cm⁻¹ resolution and typically averaged 100 times.

X-ray Diffraction under Pressure. Experiments were carried out using a membrane diamond anvil cell equipped with Boehler-type anvils with 500 μm culets. A stainless-steel gasket of 200 μm thickness was preindented to 70 μm , provided with a 200 μm hole, and loaded with the sample, a 4:1 methanol–ethanol pressure transmitting medium and a 10 μm diameter ruby sphere, which served as the pressure marker. The “Mao hydrostatic” pressure scale was used to determine pressures. X-ray powder diffraction measurements were performed at the XRD platform of the IMPMC on a Rigaku MM007HF diffractometer equipped with a Mo rotating anode ($\lambda_{K\alpha 1} = 0.709319 \text{ \AA}$, $\lambda_{K\alpha 2} = 0.713609 \text{ \AA}$), VariMax focusing optics, and a RAXIS4++ image plate detector. X-ray data were collected at 20 °C. A LaB₆ standard sample was measured in the same experimental condition to calibrate the Fit2D program, and image processing software was used to integrate

the intensities around the Debye–Scherrer rings and to get the 1D patterns.

Infrared Spectroscopy under Pressure. Membrane diamond anvil cells (DACs), equipped with IIas-type diamonds having 400–500 μm culets, are used. Stainless steel gaskets with a thickness of 200 μm are indented down to 50 μm . A 150 μm hole is then drilled by electroerosion. The gasket is placed on the top of one of the DAC diamonds, and the gasket hole is filled with NaCl. After introducing a ruby crystal, the DAC is closed under gentle pressure until the salt forms a clear window. A drop of a diluted suspension of NCs in toluene is then added and dried on top of the NaCl window to form a dry and uniform film of NCs. The DAC is then closed and introduced in a Cassegrain microscope. The pressure is generated by means of a metallic membrane inflated with He gas. The in situ pressure is monitored by the ruby luminescence technique. A 532 nm laser is shone through one of the Cassegrain objectives and focused on the ruby crystal embedded in the cell. Ruby photoluminescence is collected and sent to an Ocean Optics spectrometer, showing a characteristic doublet around 694 nm at ambient pressure. This photoluminescence is fitted, and the pressure is computed using the main peak position. Once the pressure is stabilized, an infrared absorbance spectrum is acquired using a Thermo Fisher Nicolet iS50 FTIR with a globar source, a quartz beam splitter, and a silicon detector in a transmission configuration. This operation is repeated for various pressure values from 0 GPa to 4 GPa. When the maximum pressure is reached, the membrane is deflated and several spectra are acquired to check the reversibility of the pressure effect.

k.p Modeling and Simulations. Hamiltonian matrices 3×3 and 14×14 $\mathbf{k.p}$ $H(k, T, P)$ are processed symbolically and diagonalized numerically for each couple of temperature and pressure (T, P) using the parameters in Table 1. Bulk material energy dispersion diagrams $E(k)$ are calculated using the wave vector k as a free-varying independence variable. On the contrary, spectroscopic energies of the form $E(T, P)$ are extracted by modifying k , with the following procedure. Since thermal dilation or pressure contraction occurs, the nanoparticles are implicitly labeled by their discretized wave vector $k_0 = 2\pi/L_0$ in (0 K, 0 GPa) conditions. Based on the starting energy E_{Start} in the starting conditions ($T_{\text{Start}}, P_{\text{Start}}$), the dispersion relation $E(k)$ is first inverted giving out a reference wave vector k_{Start} . This k_{Start} wavevector is then dilated or contracted back to (0 K, 0 GPa) conditions following equation S6b, thus giving the k_0 wavevector labeling the nanoparticle. The temperature T and pressure P are then freely scanned. For each (T, P), the norm of the discretized wave vector k_0 is changed into $k(k_0, T, P)$ according to the dilation or contraction of the lattice parameter. The $\mathbf{k.p}$ matrix is finally numerically evaluated at this altered wave vector k , and the eigen energies are reported against T and/or P .

RESULTS AND DISCUSSION

From Weak to Strong Confinement in HgTe Nanocrystals. We grow a series of HgTe NCs with various sizes to widely tune the confinement energy. As a strongly confined form of HgTe, 2D NPLs are grown.¹⁵ The HgTe NPLs are obtained using a two-step approach where CdTe NPLs are first synthesized,³³ see Figure S1. The NPLs are 3 monolayers thick (three planes of Te surrounded by four planes of Cd) corresponding to a thickness of 1.1 nm.³³ Those NPLs are then exposed to a bulky Hg precursor (Hg-amine complexes), which transforms them into pure HgTe NPLs due to cation exchange.¹⁵ Given that CdTe (0.648 nm) and HgTe (0.646 nm³⁴) have similar lattice parameters (0.3% difference), the final thickness of the HgTe NPL is 1.1 nm,¹⁵ which is confirmed by the fact that the two types of material present similar X-ray diffractogram, see Figure S2.

The lateral extension of the particles is large and can reach several hundreds of nanometers according to electronic microscopy, see Figure 2a and Figures S3–S5. Due to the thickness, the material is strongly confined along the $\langle 001 \rangle$ crystal direction, and the band edge absorption appears around 900 nm ($\approx 11,000 \text{ cm}^{-1}$ or $\approx 1.4 \text{ eV}$ at room temperature), see Figure 2c. It has been demonstrated that the exact value of the band-edge energy can be further tuned with the capping ligands, which also take part in the effective delocalization length.¹⁵ This enables a fine-tuning of the confinement energy while keeping the inorganic core unchanged.

In addition, we grow a series of HgTe NCs with room-temperature band edge between 9000 cm^{-1} (1.11 eV) and 2000 cm^{-1} (248 meV), see Figure 2b,c and Figure S6. The syntheses follow the procedure of Keuleyan et al.³⁵ (for large NCs) and Geiregat et al.³⁶ (for the smallest NCs). The combination of the HgTe NPLs and NCs allows us to tune the confinement energies over more than a factor of 5, from strongly to weakly confined materials as we switch from NPLs to NCs.

Effect of Temperature on the Infrared Absorption.

We then probe the effect of temperature on the IR spectrum of the materials, see the spectra given in Figure 3a–c and Figures S8 and S9. The temperature dependence of the material is

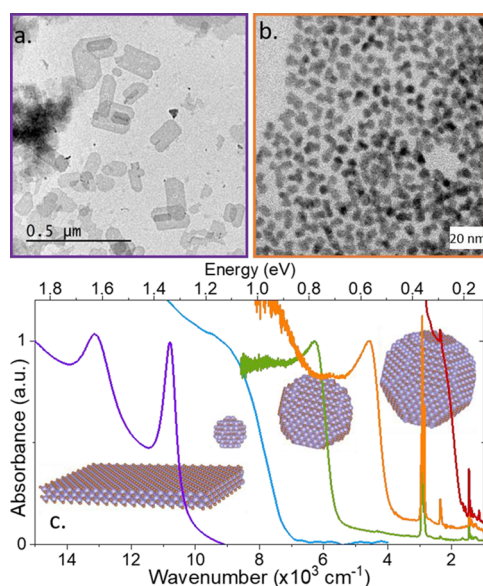


Figure 2. Confined NCs of HgTe. TEM images of (a) HgTe NPLs and (b) NCs. The associated absorption spectrum appears in purple and orange, respectively. (c) Infrared absorption spectra for HgTe NPLs and NCs with various sizes.

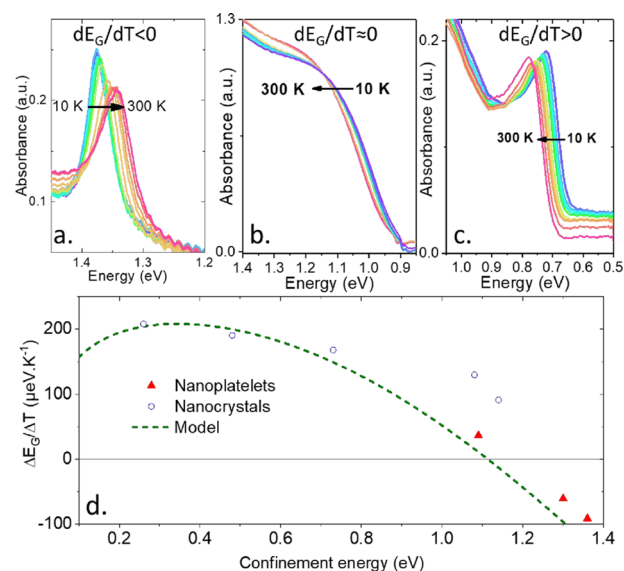


Figure 3. Effect of temperature on the infrared spectra of HgTe NCs. (a) Infrared absorption spectra for HgTe NPLs at various temperatures between 10 and 300 K. The absorption blueshifts as the temperature is lowered. (b) Infrared absorption spectra for small HgTe NCs at various temperatures between 10 and 300 K. The absorption is barely affected by temperature. (c) Infrared absorption spectra for large HgTe NCs at various temperatures between 10 and 300 K. The absorption redshifts as the temperature is lowered. (d) Experimental temperature dependence of the band gap variation as a function of HgTe NC and NPL E_G confinement energy (at $T = 10 \text{ K}$). The green dotted line is from the (3 + 1) $\mathbf{k.p}$ model.

dramatically influenced by the material confinement, as shown in Figure 3a–c. For large (i.e., weakly confined) HgTe NCs (Figure 3c), the E_G confinement energy redshifts as the temperature is lowered, corresponding to a positive value for dE_G/dT . This behavior is similar to the one observed in bulk HgTe,^{37,38} but it is opposite to the trend observed for wider band gap II–VI semiconductors such as CdTe³⁹ or CdSe.^{40,41}

where whatever the particle size, only negative values have been observed for dE_G/dT . In NCs, such positive value for dE_G/dT has been observed for lead halide perovskites⁴² or large PbS NCs.⁴³ Nevertheless, as the confinement is increased, we observe a reduction of the value of dE_G/dT (Figure 3b) and surprisingly even an inversion of its sign in the case of NPLs (Figure 3a).

This change of sign for dE_G/dT excludes that the observed shifts may result solely from a thermal dilation or contraction of the nanoparticles, the size of which will itself tune the confinement. In addition, this contribution of temperature has been found to be quantitatively weak (few $\mu\text{eV}\cdot\text{K}^{-1}$)²³ due to the very small thermal dilation, see Figure S11b. Note that the dimensionality does not seem to be a driving parameter for the magnitude of dE_G/dT since NCs (0D) and NPLs (2D) with the same E_G confinement energy present similar values for dE_G/dT , see circles and triangles in Figure 3d. A similar trend for dE_G/dT (reduction of the amplitude and change of sign) as a function of the inverse of the particle size was observed in the case of PbS NCs. By excluding other possibilities, the band gap shift with temperature was finally attributed to a size-dependent electron–phonon coupling.^{23,43}

Effect of Pressure on the Infrared Absorption.

Similarly, we measured the pressure dependence of the band gap for the HgTe NPLs at various fixed temperatures. Note that for HgTe NCs, the pressure dependence of the band gap was already reported in ref 44. at room temperature. This is why the effect of pressure is discussed in the case of NPLs here. In practice, the sample is loaded in a diamond anvil cell together with NaCl, which is used as an infrared transparent pressure transmission medium. A ruby is also loaded in the cell and used to determine the applied pressure, see Figure 4a for a scheme of the experiment and the Supporting Information for details. All the reported observations appear to be fully reversible in the targeted range of pressure (i.e., zero pressure spectrum is recovered after pressure release). On the other hand, the process is strongly hysteretic: the full release of pressure is required to recover the initial spectrum.

To understand pressure-induced change in the infrared spectrum, it is first necessary to determine if the changes are the result of a structural phase transition. Bulk HgTe crystallizes in the cubic zinc blende structure at ambient pressure and undergoes several phase changes as pressure is increased. For bulk material, the cinnabar phase appears around 1.4 GPa.^{45,46} Under NC form, the zinc-blende phase remains stable up to higher pressures.⁴⁴ In the range between 3 and 5 GPa, we can notice the presence of both zinc-blende and the cinnabar phase (Figure S7). It is, however, unclear if the two phases exist within the same NPL or if the signal is associated with different particles. In the zinc-blende phase, we identify a decrease in the lattice parameter with initial pressure ($da/dP \approx 7$ pm/GPa), which corresponds to a bulk modulus of 30 GPa for the HgTe NPLs. This value is similar to the one measured for the HgTe NCs⁴⁶ (33 GPa), which was relatively close to the one of the bulk (34 GPa).⁴⁷

The E_G confinement energy appears to be dependent on the applied pressure, see Figures 4b,c, and 6c and Figure S10. The confinement energy gradually increases with pressure corresponding to a positive value for dE_G/dP . This is similar to what has been measured for HgTe NCs,⁴⁴ and wider band gap II–VI semiconductor quantum dots such as CdSe⁴⁸ and core-shells made of CdSe/ZnS.^{49,50} Applying pressure in the range of existence of the zinc-blende phase can lead to a shift of the

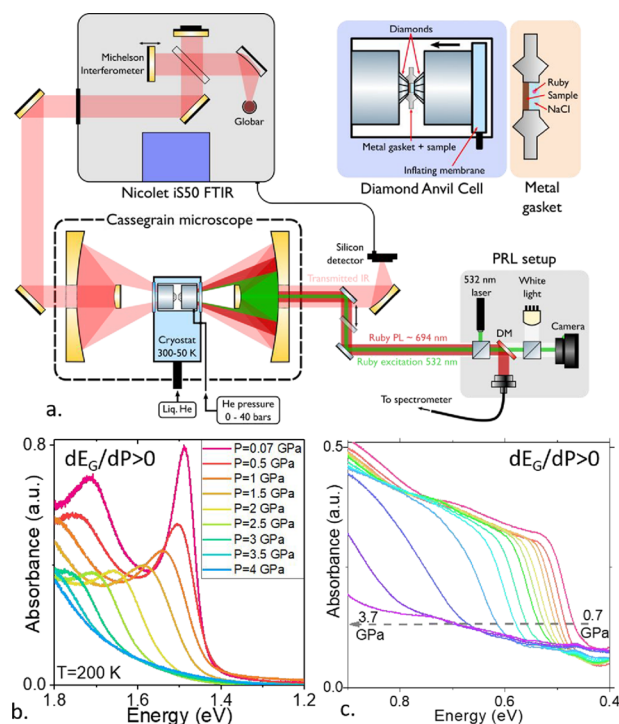


Figure 4. Effect of the pressure on the infrared spectra of HgTe NCs. (a) Scheme of the experimental setup of the SMIS beamline of synchrotron SOLEIL to probe the infrared spectrum of a HgTe NPLs under pressure. (b) Infrared spectrum of HgTe NPLs at 200 K and under various pressure in the range of 0–4 GPa. (c) Infrared spectrum of HgTe NCs at 300 K and under various pressure in the range of 0 to 4 GPa.

confinement energy up to 300 meV, which is far more than the shift induced by cooling the sample from room temperature to cryogenic conditions (≈ 35 meV). This order of magnitude is partially expected from the lattice parameter change under pressure around 6% as shown in Figure S7c and estimated around only 0.08% over 300 K temperature range as shown in Figure S11b. Above 4 GPa, no excitonic feature is identified. This observation is correlated to the disappearance of the zinc-blende phase under similar pressure, see Figure S7.

Multiband $k\cdot p$ Modelling. In order to address the striking temperature and pressure dependence of the spectra observed in Figure 3 and 4, we model the nanoparticle energies using multiband $k\cdot p$ simulations. HgTe dispersion appears to be nonparabolic,^{26,51} and the effective mass approximation (1 band model) is only valid over 1% of the Brillouin zone. For the wavevectors far away from the Γ point, the dispersion becomes first linear and then slightly bends down for wavevectors corresponding to the confinement of NPLs (confinement energy above 1 eV). More bands need to be included in the $k\cdot p$ model to obtain an accurate description of the dispersion relation.

When a detailed description of the valence band is required, an 8-band $k\cdot p$ model describing the Γ_6 , Γ_7 , and Γ_8 bands and their degeneracy is used.^{52,53} It has been estimated that the 8-band $k\cdot p$ model correctly described the Brillouin zone over 8% of it, corresponding to energies significantly smaller than the NPL ones that are around 1.1–1.8 eV.⁵² While the effective mass approximation describes only the very bottom parabolic part of the light hole like (Γ_8) band, the inclusion of an

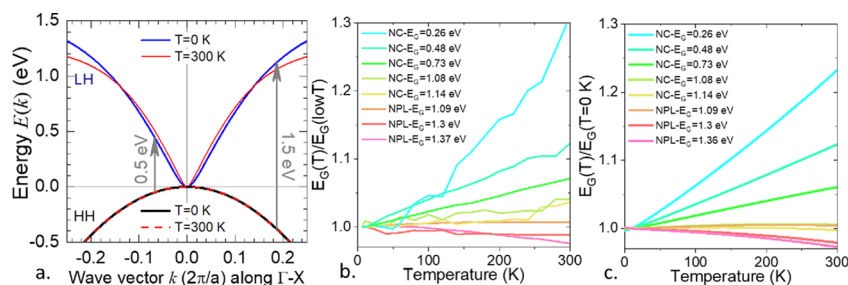


Figure 5. Modeling the temperature effect of the dispersion relation. (a) Effect of temperature on $E(k)$ when the two band gaps E_g and E_{gC} vary. The gray arrows correspond to typical confinement energies for the NPLs (1.5 eV) and for NCs (0.5 eV). (b) Experimental normalized shift of the band gap as a function of temperature for different 10 K sizes of HgTe NCs and 3 ML HgTe NPLs with different surface chemistries. (c) Simulated normalized shift of the confinement energy E_G as a function of temperature for different sizes of HgTe NCs and 3 ML HgTe NPLs with different surface chemistries.

additional conduction band is critical to capture the linear dispersion occurring at larger wavevectors and higher energies.

In HgTe, contrary to PbS, the hole and electron effective masses strongly differ, the valence band mass being more than 10 times the conduction band mass. Therefore, the confinement is mostly the result of the conduction band and the latter is the one requiring the most accuracy. In the Supporting Information (Figures S14–S17), we provide a 14-band \mathbf{k}, \mathbf{p} model, which includes the minimum amount of bands to properly take into account additional conduction bands.⁵⁴

This 14-band model aims at supporting a simpler (3 + 1) effective bands model later described in the main text. This simple model provides the driving concepts leading to the realistic calculated 14-band structure. The 14-band model includes notably the spin-orbit coupling, disregarded in the simplified model, and all relevant interactions. Note that Coulombic renormalization of the band gap has been neglected since these effects have been found to be small in the case of HgTe NCs.²⁶ Even though the conclusions are qualitatively the same using each version of the model, the complete version may somehow blur the message with a large amount of involved parameters. This is why, in the following text, we describe a simplified approach. We use a (3 + 1) band one-dimensional \mathbf{k}, \mathbf{p} -like model, referred to as the simple model and described in the Supporting Information. Its illustrative role is to be tractable and to account for all the experimental features with a minimal set of necessary ingredients, as defined and shown in Figure 1. The associated parameters are given in Table 1.

The (3 + 1) band model accounts for the two bands with Γ_8 symmetry at $k \rightarrow 0$ (called HH and LH in Figure 1) which are the bands around the Fermi level and involved in the absorption. We also include the Γ_6 valence band and a second conduction band. The introduction of this effective high-energy band in the conduction band is central to accurately describe the bending of the LH band occurring at large wavevectors.

All the experimental data are then accounted from the variation with temperature and pressure of only two bulk band gap energies: $E_g(T, P)$ and $E_{gC}(T, P)$. As these gaps will be affected by pressure and temperature, the band curvature will be modified (through the E_p and E_{pC} parameters coupling the bands), unveiling the effect of pressure and temperature in the presence of confinement (i.e., away from the Γ point). The strong confinement in the HgTe nanoparticles is modeled by the discretization of the $k \rightarrow$ wavevector in the reciprocal space, typically at $k = \pm \frac{\pi}{L}$ along [001], where L is the size of the

nanoparticle, accounting for the contraction and thermal dilation of the nanoparticle with pressure and temperature, respectively.

Figures 5a and 6a, respectively, show the effects of temperature and pressure on the relation dispersion. When

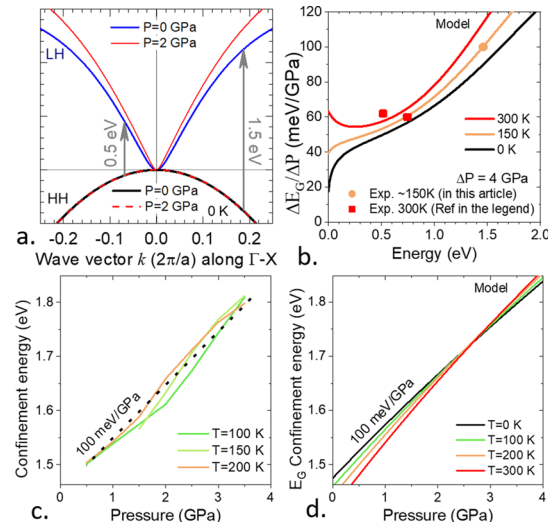


Figure 6. Modeling the pressure effect of the dispersion relation (a) Effect of pressure on the conduction and valence bands. The gray arrows correspond to typical confinement energies for the NPL (1.5 eV) and for NCs (0.5 eV). (b) Simulated confinement energy variation over $\Delta P=4$ GPa pressure difference for 3 temperatures. The light orange dot is the experimental measurement around 150 K. The two red squares are the measurements from Ref 44 at 300 K. (c) Experimental confinement energy E_{gC} shifts as a function of an applied hydrostatic pressure for HgTe NPLs for three different temperatures. (d) Simulated confinement energy E_{gC} shifts as a function of an applied pressure for HgTe NPLs from 0 to 300 K. The indicated slope corresponds to 0 K.

temperature or pressure increases, the band gaps E_g and E_{gC} are altered as shown in Figure S11c. The effect on the LH band effective mass m_{LH}^* , defined at small k , is given by:

$$E_{LH}(k, T, P) \simeq \left(1 + \frac{E_p}{E_g(T, P)} - \frac{E_{pC}}{E_{gC}(T, P)} \right) \frac{\hbar^2 k^2}{2m_0} = \frac{\hbar^2 k^2}{2m_{LH}^*} \quad (1)$$

As seen in eq 1, these variations lead to a competition between the two gaps $E_g(T,P)$ and $E_{gC}(T,P)$ in the alteration of $E_{LH}(k)$ relation dispersion.

At low energy (i.e., small k , see the left arrow in the dispersion relation), the dispersion is ruled by the m_{LH}^* effective mass reduction. The energy blueshift as shown in Figure 5a for temperature, and Figure 6a for pressure is the result of the drastic reduction of E_g from 0.31 eV at 0 K down to 0.12 eV at room temperature. E_g being one order of magnitude smaller than E_{gC} , and $\partial E_g/\partial T/E_g$ and $\partial E_{gC}/\partial T/E_{gC}$ partial derivatives being comparable, the effective mass is essentially governed by E_g (i.e., the second conduction band plays no role in the vicinity of the Γ point). The same rule of thumb holds for pressure.

However, at high energies (i.e., high k , see the right arrow in the dispersion relation), the parabolic eq 1 ceases to be valid. When temperature increases, the second conduction band counteracts m_{LH}^* reduction. As a result of the shrinking of E_{gC} , the second conduction band becomes closer to the LH band and repeals it downward as seen in Figure 5a. In other words, the second conduction band is responsible for the sublinear relation dispersion observed at large k and leads to an inversion of the confinement energy variation with a simulated redshift of the E_G confinement energy.

Using the (3 + 1) band model and $-2.4 \text{ meV}\cdot\text{K}^{-1}$ value for $\frac{\partial E_{gC}}{\partial T}$, the experimental temperature dependence of the band gap (Figure 5b) is reproduced, as shown in Figure 5c. With $low T = 10 \text{ K}$, the blueshift ($E_G(T)/E_G(low T) > 1$) at small energies is due to the shrinking of the E_g band gap. However, at large energies, E_{gC} also shrinks and the closer second conduction band pushes the first one downward, leading to a redshift ($E_G(T)/E_G(low T) < 1$). This interpretation is further analyzed quantitatively by plotting the simulated slopes $\frac{\Delta E_G}{\Delta T}$ as a function of the confinement energy of the particles, see the dashed green line in Figure 3d. We see that the model appears in fair agreement with the observed slopes over the whole range of experimental energies supporting the interpretation of the shrinking of the two gap energies.

Regarding the pressure dependence, the observed energy shifts with hydrostatic pressure present an average slope $\frac{\Delta E_G}{\Delta P} \approx 100 \text{ meV/GPa}$ in the case of NPLs (Figures 4b, 6c, and Figure S10) which has to be compared with the value of $\approx 60 \text{ meV/GPa}$ for the nanocrystals⁴⁴ (Figure 4c and Figure S13). Contrary to the case of temperature, the confinement only quantitatively affects the pressure dependence of the confinement energy. This result contrasts to CdSe where the size dependence of the $\frac{\Delta E_G}{\Delta P}$ parameter has been found to be larger with an increase of $\frac{\Delta E_G}{\Delta P}$ from 40 to 80 meV/GPa as the size changes by only a factor of 2.⁴⁸

Under increasing pressure, the second conduction band goes away from the first one. Pressure simply pushes E_G confinement energy even higher, see Figure 6a. In this case, due to pressure, the second conduction band adds an additional contribution to the one of E_g to the observed blueshift of the confinement energy E_G .

Using -85 meV/GPa and $+220 \text{ meV/GPa}$, respectively, for $\partial E_g/\partial P$ and $\partial E_{gC}/\partial P$, the (3 + 1) bands model can reproduce the pressure dependence of the confinement energy of the NPLs, see Figure 6c and d. Also note that using the temperature dependence determined previously, it is possible

to reproduce the weak temperature dependence of the pressure potential dE_G/dP of the confinement energy in the case of NPLs, see the four simulated temperatures in Figure 6d, while capturing the moderate confinement dependence as depicted in Figure 6b and Figure S13a.

In all, though both temperature and pressure alter the bulk band gaps E_g and E_{gC} , only blue shifts are observed with increasing pressure, while increasing temperature also shows red shifts. We thus conclude that the unusual change of the optical band gap with temperature and its change of sign reflects the bulk material electronic structure and that phonon does not have to be invoked.⁴³

CONCLUSIONS

In conclusion, we have shown that the strong confinement in NPLs causes a nonlinear dispersion of high energy state energies in the electronic structure of HgTe nanoparticles. Measurements of the temperature dependence of the optical band gap appears as a direct probe of the dispersion relation. We found that a single parameter set in the (3 + 1) effective band model can account for all the observed features in energy, temperature, and pressure, providing that the relative proximity of the second conduction band of HgTe is included. We show that the second conduction band appears as a paramount ingredient for absorption energies above $\approx 0.5\text{--}1 \text{ eV}$ to describe realistically the energies and electronic states of strongly confined HgTe nanoparticles.

ASSOCIATED CONTENT

Supporting Information

The Supporting Information is available free of charge at <https://pubs.acs.org/doi/10.1021/acs.jpcc.0c07533>.

Material synthesis, material characterization, X-ray diffraction measurement under pressure, raw spectrum of material temperature and pressure dependence and additional information regarding the (3 + 1)-band **k,p**-like and 14 band **k,p** models (PDF)

AUTHOR INFORMATION

Corresponding Authors

Sébastien Sauvage – Université Paris-Saclay, CNRS, Centre de Nanosciences et de Nanotechnologies, 91120 Palaiseau, France;

orcid.org/0000-0001-8132-1372;

Email: sebastien.sauvage@c2n.upsaclay.fr

Emmanuel Lhuillier – Sorbonne Université, CNRS, Institut des NanoSciences de Paris, INSP, F-75005 Paris, France;

orcid.org/0000-0003-2582-1422; Email: el@insp.upmc.fr

Authors

Nicolas Moghaddam – Laboratoire de Physique et d'Etude des Matériaux, ESPCI-ParisTech, Sorbonne Université, 75005 Paris, France; orcid.org/0000-0003-2935-9386

Charlie Gréboval – Sorbonne Université, CNRS, Institut des NanoSciences de Paris, INSP, F-75005 Paris, France;

orcid.org/0000-0002-0314-7273

Junling Qu – Sorbonne Université, CNRS, Institut des NanoSciences de Paris, INSP, F-75005 Paris, France;

orcid.org/0000-0003-2504-1274

Audrey Chu – Sorbonne Université, CNRS, Institut des NanoSciences de Paris, INSP, F-75005 Paris, France;

orcid.org/0000-0002-6905-7131

Prachi Rastogi – Sorbonne Université, CNRS, Institut des NanoSciences de Paris, INSP, F-75005 Paris, France;

orcid.org/0000-0003-3535-0441

Clément Livache – Sorbonne Université, CNRS, Institut des NanoSciences de Paris, INSP, F-75005 Paris, France;

orcid.org/0000-0002-2588-2607

Adrien Khalili – Laboratoire de Physique et d'Etude des Matériaux, ESPCI-ParisTech, Sorbonne Université, 75005 Paris, France; orcid.org/0000-0001-5685-9963

Xiang Zhen Xu – Laboratoire de Physique et d'Etude des Matériaux, ESPCI-ParisTech, Sorbonne Université, 75005 Paris, France

Benoit Baptiste – Sorbonne Université, CNRS, Institut de Minéralogie, de Physique des Matériaux et de Cosmochimie, IMPMC, F-75005 Paris, France

Stefan Klotz – Sorbonne Université, CNRS, Institut de Minéralogie, de Physique des Matériaux et de Cosmochimie, IMPMC, F-75005 Paris, France

Guy Fishman – Kadope, Centre de Nanosciences et de Nanotechnologies, 91120 Palaiseau, France

Francesco Capitani – Synchrotron SOLEIL, L'Orme des Merisiers, Saint-Aubin, 91192 Gif sur Yvette, France;

orcid.org/0000-0003-1161-7455

Sandrine Ithurria – Laboratoire de Physique et d'Etude des Matériaux, ESPCI-ParisTech, Sorbonne Université, 75005 Paris, France; orcid.org/0000-0002-4733-9883

Complete contact information is available at:
<https://pubs.acs.org/10.1021/acs.jpcc.0c07533>

Notes

The authors declare no competing financial interest.

ACKNOWLEDGMENTS

We thank Mayank Goyal for participation to synchrotron experiments. This work has been supported by the Region Ile-de-France in the framework of DIM Nano-K (grant dopQD). This work was supported by French state funds managed by the ANR within the Investissements d'Avenir programme by Labex Matisse (ANR-11-IDEX-0004-02), and Labex Nano-Saclay (ANR-10-LABX-0035), and also by the grant FRONTAL (ANR-19-CE09-0017), IPER-Nano2 (ANR-18-CE30-0023-01), Copin (ANR-19-CE24-0022), Graskop (ANR-19-CE09-0026). J.Q. thanks Chinese Scholar council for PhD grant and A.C. thanks Agence Innovation Defense. E.L. thanks the support ERC starting grant blackQD (grant n° 756,225). S.I. thanks the support ERC starting grant Ne2Dem (grant n° 853,049).

REFERENCES

- (1) Bourzac, K. Quantum Dots Go on Display. *Nature* **2013**, *493*, 283.
- (2) Green, M.; Mirzai, H. Synthetic Routes to Mercury Chalcogenide Quantum Dots. *J. Mater. Chem. C* **2018**, *6*, 5097–5112.
- (3) Nozik, A. J. Quantum Dot Solar Cells. *Phys. E Low-Dimens. Syst. Nanostructures* **2002**, *14*, 115–120.
- (4) McDonald, S. A.; Konstantatos, G.; Zhang, S.; Cyr, P. W.; Klem, E. J. D.; Levina, L.; Sargent, E. H. Solution-Processed PbS Quantum Dot Infrared Photodetectors and Photovoltaics. *Nat. Mater.* **2005**, *4*, 138–142.
- (5) Hafiz, S. B.; Scimeca, M.; Sahu, A.; Ko, D.-K. Colloidal Quantum Dots for Thermal Infrared Sensing and Imaging. *Nano Converg.* **2019**, *6*, 7.

(6) Livache, C.; Martinez, B.; Goubet, N.; Ramade, J.; Lhuillier, E. Road Map for Nanocrystal Based Infrared Photodetectors. *Front. Chem.* **2018**, *6*, 575.

(7) Lhuillier, E.; Guyot-Sionnest, P. Recent Progresses in Mid Infrared Nanocrystal Optoelectronics. *IEEE J. Sel. Top. Quantum Electron.* **2017**, *23*, 6000208.

(8) Böberl, M.; Kovalenko, M. V.; Gamerith, S.; List, E. J. W.; Heiss, W. Inkjet-Printed Nanocrystal Photodetectors Operating up to 3 μm Wavelengths. *Adv. Mater.* **2007**, *19*, 3574–3578.

(9) Cryer, M. E.; Halpert, J. E. 300 nm Spectral Resolution in the Mid-Infrared with Robust, High Responsivity Flexible Colloidal Quantum Dot Devices at Room Temperature. *ACS Photonics* **2018**, *5*, 3009–3015.

(10) Chu, A.; Martinez, B.; Ferré, S.; Noguier, V.; Gréboval, C.; Livache, C.; Qu, J.; Prado, Y.; Casaretto, N.; Goubet, N.; et al. HgTe Nanocrystals for SWIR Detection and Their Integration up to the Focal Plane Array. *ACS Appl. Mater. Interfaces* **2019**, *11*, 33116–33123.

(11) Chatterjee, A.; Pendyala, N. B.; Jagtap, A.; Rao, K. S. R. K. Uncooled Mid-Wave Infrared Focal Plane Array Using Band Gap Engineered Mercury Cadmium Telluride Quantum Dot Coated Silicon ROIC. *E-J. Surf. Sci. Nanotechnol.* **2019**, *17*, 95–100.

(12) Buurma, C.; Pimpinella, R. E.; Ciani, A. J.; Feldman, J. S.; Grein, C. H.; Guyot-Sionnest, P. MWIR Imaging with Low Cost Colloidal Quantum Dot Films. In *Optical Sensing, Imaging, and Photon Counting: Nanostructured Devices and Applications 2016*; International Society for Optics and Photonics, 2016; 993303.

(13) Lhuillier, E.; Scarafagio, M.; Hease, P.; Nadal, B.; Aubin, H.; Xu, X. Z.; Lequeux, N.; Patriarche, G.; Ithurria, S.; Dubertret, B. Infrared Photodetection Based on Colloidal Quantum-Dot Films with High Mobility and Optical Absorption up to THz. *Nano Lett.* **2016**, *16*, 1282–1286.

(14) Goubet, N.; Jagtap, A.; Livache, C.; Martinez, B.; Portalès, H.; Xu, X. Z.; Lobo, R. P. S. M.; Dubertret, B.; Lhuillier, E. Terahertz HgTe Nanocrystals: Beyond Confinement. *J. Am. Chem. Soc.* **2018**, *140*, 5033–5036.

(15) Izquierdo, E.; Robin, A.; Keuleyan, S.; Lequeux, N.; Lhuillier, E.; Ithurria, S. Strongly Confined HgTe 2D Nanoplatelets as Narrow Near-Infrared Emitters. *J. Am. Chem. Soc.* **2016**, *138*, 10496–10501.

(16) Tenney, S. M.; Vilchez, V.; Sonnleitner, M. L.; Huang, C.; Friedman, H. C.; Shin, A. J.; Atallah, T. L.; Deshmukh, A. P.; Ithurria, S.; Caram, J. R. Mercury Chalcogenide Nanoplatelet–Quantum Dot Heterostructures as a New Class of Continuously Tunable Bright Shortwave Infrared Emitters. *J. Phys. Chem. Lett.* **2020**, *11*, 3473–3480.

(17) Chang, Y.-C.; Schulman, J. N.; Bastard, G.; Guldner, Y.; Voos, M. Effects of Quasi-Interface States in HgTe–CdTe Superlattices. *Phys. Rev. B* **1985**, *31*, 2557–2560.

(18) Rogalski, A. HgCdTe Infrared Detector Material: History, Status and Outlook. *Rep. Prog. Phys.* **2005**, *68*, 2267–2336.

(19) Orłowski, N.; Augustin, J.; Gołacki, Z.; Janowitz, C.; Manzke, R. Direct Evidence for the Inverted Band Structure of HgTe. *Phys. Rev. B* **2000**, *61*, R5058–R5061.

(20) Bernevig, B. A.; Hughes, T. L.; Zhang, S.-C. Quantum Spin Hall Effect and Topological Phase Transition in HgTe Quantum Wells. *Science* **2006**, *314*, 1757–1761.

(21) König, M.; Wiedmann, S.; Brüne, C.; Roth, A.; Buhmann, H.; Molenkamp, L. W.; Qi, X.-L.; Zhang, S.-C. Quantum Spin Hall Insulator State in HgTe Quantum Wells. *Science* **2007**, *318*, 766–770.

(22) Leubner, P.; Lunczer, L.; Brüne, C.; Buhmann, H.; Molenkamp, L. W. Strain Engineering of the Band Gap of HgTe Quantum Wells Using Superlattice Virtual Substrates. *Phys. Rev. Lett.* **2016**, *117*, No. 086403.

(23) Lhuillier, E.; Keuleyan, S.; Guyot-Sionnest, P. Optical Properties of HgTe Colloidal Quantum Dots. *Nanotechnology* **2012**, *23*, 1750705.

(24) Chen, M.; Guyot-Sionnest, P. Reversible Electrochemistry of Mercury Chalcogenide Colloidal Quantum Dot Films. *ACS Nano* **2017**, *11*, 4165–4173.

- (25) Hudson, M. H.; Chen, M.; Kamysbayev, V.; Janke, E. M.; Lan, X.; Allan, G.; Delerue, C.; Lee, B.; Guyot-Sionnest, P.; Talapin, D. V. Conduction Band Fine Structure in Colloidal HgTe Quantum Dots. *ACS Nano* **2018**, *12*, 9397–9404.
- (26) Allan, G.; Delerue, C. Tight-Binding Calculations of the Optical Properties of HgTe Nanocrystals. *Phys. Rev. B* **2012**, *86*, 165437.
- (27) Keuleyan, S. E.; Guyot-Sionnest, P.; Delerue, C.; Allan, G. Mercury Telluride Colloidal Quantum Dots: Electronic Structure, Size-Dependent Spectra, and Photocurrent Detection up to 12 μm . *ACS Nano* **2014**, *8*, 8676–8682.
- (28) Jagtap, A.; Martinez, B.; Goubet, N.; Chu, A.; Livache, C.; Gréboval, C.; Ramade, J.; Amelot, D.; Troussset, P.; Triboulin, A.; et al. Design of a Unipolar Barrier for a Nanocrystal-Based Short-Wave Infrared Photodiode. *ACS Photonics* **2018**, *5*, 4569–4576.
- (29) Izquierdo, E.; Dufour, M.; Chu, A.; Livache, C.; Martinez, B.; Amelot, D.; Patriarche, G.; Lequeux, N.; Lhuillier, E.; Ithurria, S. Coupled HgSe Colloidal Quantum Wells through a Tunable Barrier: A Strategy To Uncouple Optical and Transport Band Gap. *Chem. Mater.* **2018**, *30*, 4065–4072.
- (30) Gréboval, C.; Izquierdo, E.; Livache, C.; Martinez, B.; Dufour, M.; Goubet, N.; Moghaddam, N.; Qu, J.; Chu, A.; Ramade, J.; et al. Impact of Dimensionality and Confinement on the Electronic Properties of Mercury Chalcogenide Nanocrystals. *Nanoscale* **2019**, *11*, 3905–3915.
- (31) Goubet, N.; Livache, C.; Martinez, B.; Xu, X. Z.; Ithurria, S.; Royer, S.; Cruguel, H.; Patriarche, G.; Ouerghi, A.; Silly, M.; et al. Wave-Function Engineering in HgSe/HgTe Colloidal Heterostructures To Enhance Mid-Infrared Photoconductive Properties. *Nano Lett.* **2018**, *18*, 4590–4597.
- (32) Pedetti, S.; Nadal, B.; Lhuillier, E.; Mahler, B.; Bouet, C.; Abécassis, B.; Xu, X.; Dubertret, B. Optimized Synthesis of CdTe Nanoplatelets and Photoresponse of CdTe Nanoplatelets Films. *Chem. Mater.* **2013**, *25*, 2455–2462.
- (33) Pedetti, S.; Ithurria, S.; Heuclin, H.; Patriarche, G.; Dubertret, B. Type-II CdSe/CdTe Core/Crown Semiconductor Nanoplatelets. *J. Am. Chem. Soc.* **2014**, *136*, 16430–16438.
- (34) Śniadower, L.; Psoda, M.; Gałazka, R. R. X-Ray Measurements of Lattice Dilatation in HgTe. *Phys. Status Solidi B* **1968**, *28*, K121–K123.
- (35) Keuleyan, S.; Lhuillier, E.; Guyot-Sionnest, P. Synthesis of Colloidal HgTe Quantum Dots for Narrow Mid-IR Emission and Detection. *J. Am. Chem. Soc.* **2011**, *133*, 16422–16424.
- (36) Geiregat, P.; Houtepen, A. J.; Sagar, L. K.; Infante, I.; Zapata, F.; Grigel, V.; Allan, G.; Delerue, C.; Van Thourhout, D.; Hens, Z. Continuous-Wave Infrared Optical Gain and Amplified Spontaneous Emission at Ultralow Threshold by Colloidal HgTe Quantum Dots. *Nat. Mater.* **2018**, *17*, 35–42.
- (37) Guenzer, C. S.; Bienenstock, A. Temperature Dependence of the HgTe Band Gap. *Phys. Rev. B* **1973**, *8*, 4655–4667.
- (38) Dobrowolska, M.; Mycielski, A.; Dobrowolski, W. Determination of Temperature Dependence of Energy Gap in HgTe by Oscillatory Magnetotransmission Measurements. *Solid State Commun.* **1978**, *27*, 1233–1235.
- (39) Fonthal, G.; Tirado-Mejía, L.; Marín-Hurtado, J. I.; Ariza-Calderón, H.; Mendoza-Alvarez, J. G. Temperature Dependence of the Band Gap Energy of Crystalline CdTe. *J. Phys. Chem. Solids* **2000**, *61*, 579–583.
- (40) Ithurria, S.; Tessier, M. D.; Mahler, B.; Lobo, R. P. S. M.; Dubertret, B.; Efros, A. L. Colloidal Nanoplatelets with Two-Dimensional Electronic Structure. *Nat. Mater.* **2011**, *10*, 936–941.
- (41) Kushavah, D.; Mohapatra, P. K.; Ghosh, P. Reduced Carrier Trapping in CdSe/ZnS/CdSe Heterostructure Quantum Dots Inferred from Temperature Dependent Spectral Studies. *Phys. E Low-Dimens. Syst. Nanostructures* **2018**, *102*, 58–65.
- (42) Ramade, J.; Andriambarijaona, L. M.; Steinmetz, V.; Goubet, N.; Legrand, L.; Barisien, T.; Bernardot, F.; Testelin, C.; Lhuillier, E.; Bramati, A.; et al. Exciton-Phonon Coupling in a CsPbBr₃ Single Nanocrystal. *Appl. Phys. Lett.* **2018**, *112*, No. 072104.
- (43) Olkhovets, A.; Hsu, R.-C.; Lipovskii, A.; Wise, F. W. Size-Dependent Temperature Variation of the Energy Gap in Lead-Salt Quantum Dots. *Phys. Rev. Lett.* **1998**, *81*, 3539–3542.
- (44) Livache, C.; Goubet, N.; Gréboval, C.; Martinez, B.; Ramade, J.; Qu, J.; Triboulin, A.; Cruguel, H.; Baptiste, B.; Klotz, S.; et al. Effect of Pressure on Interband and Intraband Transition of Mercury Chalcogenide Quantum Dots. *J. Phys. Chem. C* **2019**, *123*, 13122–13130.
- (45) Wright, N. G.; McMahon, M. I.; Nemes, R. J.; San-Miguel, A. Crystal Structure of the Cinnabar Phase of HgTe. *Phys. Rev. B* **1993**, *48*, 13111–13114.
- (46) San-Miguel, A.; Wright, N. G.; McMahon, M. I.; Nemes, R. J. Pressure Evolution of the Cinnabar Phase of HgTe. *Phys. Rev. B* **1995**, *51*, 8731–8736.
- (47) Düz, I.; Erdem, I.; Ozdemir Kart, S.; Kuzucu, V. First Principles Investigations of HgX (X=S, Se and Te). *Arch Mater Sci Eng* **2016**, *79*, 5–11.
- (48) Meulenberg, R. W.; Strouse, G. F. Pressure-Induced Electronic Coupling in CdSe Semiconductor Quantum Dots. *Phys. Rev. B* **2002**, *66*, No. 035317.
- (49) Li, B.; Liu, W.; Zhu, X.; Lin, S.; Yang, Y.; Yang, Q.; Jin, P. Pressure-Dependent Photoluminescence of CdSe/ZnS Quantum Dots: Critical Point of Different Pressure Regimes. *Phys. Lett. A* **2019**, *383*, 1483–1486.
- (50) Fan, H. M.; Ni, Z. H.; Feng, Y. P.; Fan, X. F.; Kuo, J. L.; Shen, Z. X.; Zou, B. S. High Pressure Photoluminescence and Raman Investigations of CdSe/ZnS Core/Shell Quantum Dots. *Appl. Phys. Lett.* **2007**, *90*, No. 021921.
- (51) Svane, A.; Christensen, N. E.; Cardona, M.; Chantis, A. N.; van Schilfgaarde, M.; Kotani, T. Quasiparticle Band Structures of β -HgS, HgSe, and HgTe. *Phys. Rev. B* **2011**, *84*, 205205.
- (52) Man, P.; Pan, D. S. Infrared Absorption in HgTe. *Phys. Rev. B* **1991**, *44*, 8745–8758.
- (53) Pokatilov, E. P.; Fonoberov, V. A.; Fomin, V. M.; Devreese, J. T. Electron and Hole States in Quantum Dot Quantum Wells within a Spherical Eight-Band Model. *Phys. Rev. B* **2001**, *64*, 245329.
- (54) El kurdi, M.; Fishman, G.; Sauvage, S.; Boucaud, P. Comparison between 6-Band and 14-Band $k\cdot p$ Formalisms in SiGe/Si Heterostructures. *Phys. Rev. B* **2003**, *68*, 165333.
- (55) Laurenti, J. P.; Camassel, J.; Bouhemadou, A.; Toulouse, B.; Legros, R.; Lussou, A. Temperature Dependence of the Fundamental Absorption Edge of Mercury Cadmium Telluride. *J. Appl. Phys.* **1990**, *67*, 6454–6460.